Acta Geochim (2020) 39(4):574–586
https://doi.org/10.1007/s11631-019-00387-1

ORIGINAL ARTICLE

U–Pb dating and geochemistry of granite porphyry dykes in the Xicha gold–(silver) deposit, southern Jilin Province, China, and their metallogenic significance

Jian Wang[1] · **Fengyue Sun**[2] · **Bile Li**[2] · **Lihui Tian**[1]

Received: 5 June 2019 / Revised: 6 November 2019 / Accepted: 2 December 2019 / Published online: 11 December 2019
© Science Press and Institute of Geochemistry, CAS and Springer-Verlag GmbH Germany, part of Springer Nature 2019

Abstract We report U–Pb dating of zircon, as well as geochemical and Hf isotope data, in order to constrain the formation time, magma source, and tectonic setting of granite porphyry dykes in the Xicha gold–(silver) district in southern Jilin Province, Northeast China. The zircon grains are euhedral–subhedral, display oscillatory growth zoning and have Th/U ratios varying between 0.11 and 0.78, which together imply a magmatic origin. The dating results indicate the porphyry formed in the Early Cretaceous (122 ± 1 Ma), and it contains $SiO_2 = 70.64–72.31$ wt%, $Al_2O_3 = 13.99–14.64$ wt%, $K_2O + Na_2O = 6.96–7.81$ wt%, $K_2O/Na_2O = 1.24–2.10$, and A/CNK = 1.11–1.41. Chemically, the porphyry belongs to a high-K calc-alkaline S-type granite. Chondrite-normalized rare earth elements (REE) patterns show LREE enrichment, light rare earth elements (LREE)/heavy rare earth elements (HREE) = 9.93–11.97, $(La/Yb)_N = 11.08–15.16$, and δEu = 0.69–0.95. On the trace element spider diagram, large ion lithophile elements such as Rb, Ba, K, Th, and U are enriched, whereas the high field strength elements Ti and P are depleted. The εHf(t) values of zircon from the granite porphyry vary between − 17.1 and − 13.2, and their Hf two-stage model ages vary from 2.01 to 2.26 Ga, implying that the magma was derived from partial melting of old lower crust. The granite porphyry dykes and many A-type granites in the region formed at the same time, suggesting an extensional environment. The combination of the occurrence of strong magmatism, large-scale mineralization, and extensional tectonics throughout much of Eastern China indicate that the Early Cretaceous was a period of significant lithospheric thinning. The southern Jilin Province, therefore, experienced lithospheric thinning during the Early Cretaceous.

Keywords Southern Jilin Province · Syn-mineralization dykes · Jinchanggou · Zircon U–Pb geochronology · Geochemistry · Hf isotopes

1 Introduction

The study area is situated near the northeast margin of the North China Craton, which was affected by the closure of the Paleo-Asian Ocean toward the north (Sun et al. 2005; Deng et al. 2009; Guo et al. 2009; Li et al. 2009a, b) and the subduction of the Pacific Plate in the Early to Middle Jurassic. As a result of subduction and collision from multiple directions, the North China Craton became activated and experienced large-scale magmatism (Zhai et al. 2003; Wu et al. 2005a) and mineralization (Mao et al. 2003; Yang et al. 2003; Mao et al. 2005) during the Mesozoic. However, the tectonic setting and temporal-spatial range of this activity have yet to be studied in detail. Intense magmatism and mineralization also occurred during the Mesozoic in southern Jilin Province, Northeast China. However, compared with the Jiaodong area, studies

✉ Jian Wang
270903856@qq.com

Fengyue Sun
sunfy_66@126.com

Bile Li
lbl66@sina.com

Lihui Tian
2005800196@mail.usth.edu.cn

[1] School of Mining Engineering, Heilongjiang University of Science and Technology, No. 2468 Puyuan Street, Harbin 150022, People's Republic of China

[2] College of Earth Sciences, Jilin University, Changchun 130061, People's Republic of China

from the Jilin Province are lacking; consequently, a better understanding of the timing and geodynamics of metallogenesis is needed. Typical hydrothermal type gold deposits in southern Jilin Province include the Jiapigou gold deposit, the Haigou gold deposit, the Erdaodianzi gold deposit, and the Xicha gold–(silver) deposit. The Jiapigou gold deposit has been extensively studied and was formed at 170–160 Ma (Luo et al. 2002; Li et al. 2003, 2004). But, the rest of the gold deposits have not been studied in detail. The Xicha gold–(silver) deposit, located in Ji'an City, Tonghua, southern Jilin Province, is a medium-sized (about 5.3 t Au) hydrothermal vein-type gold–(silver) deposit that was discovered in the 1960s. Previous studies have considered various aspects of the Xicha deposit, including its geological characteristics and metallogenic conditions (Feng 2000). However, the age of mineralization has yet to be resolved. Feng (2000) suggested that the deposit formed in the Yanshanian, a relatively large time span, which constrains the timing of metallogenesis, the geological setting, and the geodynamic setting of mineralization. Therefore, we have studied the geochronology and geochemistry of granite porphyry dikes that are closely related to ore-forming veins in the Xicha gold–(silver) deposit. The results are combined with previously published data to constrain the age of mineralization and to provide a geochronological framework and information on the tectonic setting of mineralization.

2 Geological setting and sample descriptions

The study area is located near the northeast margin of the North China Craton (Fig. 1a). The area is adjacent to the Xingmeng orogenic belt to the north (across the Xilamulun River–Changchun–Yanji suture), the Korean Peninsula to the east, and the Liaodong Peninsula to the south, while the Dunmi Fault (the northern extension of the Tanlu fracture) and the Yalujiang Fault cut through the northwest and southeast parts of the area, respectively. Crystalline basement in the region is mainly composed of Archean tonalite trondhjemite granodiorite gneisses, the supracrustal rocks of the Paleoproterozoic Ji'an groups, and the Paleoproterozoic granites (Lu et al. 2004). The Ji'an groups consist of marble, leptynite, mica schist, amphibolite, plagioclase amphibolite, quartzite, and quartz schist. The cover rocks consist of thick Sinian–Paleozoic sedimentary strata and Mesozoic–Cenozoic volcano-sedimentary strata. In addition, Mesozoic felsic intrusive rocks occur in the region. Zircon U–Pb age data indicate that magmatic activity occurred primarily in the Late Triassic, Early–Middle Jurassic, and Early Cretaceous (Lu et al. 2003; Pei et al. 2005; Sun et al. 2005; Qin et al. 2012).

Paleoproterozoic strata are exposed in the Jinchanggou mine area (Fig. 1b); the main lithologies consist of leptynite, graphite marble, plagioclase amphibolite, leucoleptite, and olivine marble. Notably, boron is enriched in the olive marble. Structural features are strongly developed in the region. The Xiaomenggou–Sidaoyangcha anticline is the main NW–SE-trending fold and NE–SW-trending faults are the main structures that cut early magmatic rocks and folds. The F7 fault (Fig. 1b), which is the major fault in the region, strikes 15°–30° and dips at 80° to the SE. The Xicha gold–(silver) deposit is located along the F7 fault, which controlled the location of mineralization. The intrusive rocks in the region are Triassic biotite diorite, syenite granite, and granitic porphyry. The biotite diorite intrudes Paleoproterozoic strata in the core of the Xiamenggou–Sidaoyangcha anticline, with an exposed area of 16 km^2, and is a composite pluton displaying features of multi-stage intrusion. Zircon from biotite diorite yields a U–Pb age of 238 ± 1 Ma (Wang et al. 2016), and zircon from biotite diorite outcropping near the Jinchanggou deposit area yield a U–Pb age of 221 ± 1 Ma (Wang et al. 2016). There are many types of dikes in the mine area, including granite porphyry, diorite, and diabase. The granite porphyry dykes and gold-bearing veins both occur along the F7 fault and they are closely related to each other, both spatially and temporally. Gold enrichment occurs where granite porphyry dykes are most commonly developed and these dykes show varying degrees of mineralization and alteration. The granite porphyry dykes should, therefore, be considered as syn-mineralization dykes because they have a close genetic relationship with the gold-bearing veins.

The Jinchanggou ore area is composed of the Jinchanggou gold deposit and the Xicha gold–(silver) deposit. The Xicha mineralization was controlled by the F7 fault and parallel secondary faults located on either side of the F7 fault. The ore body occurs as veins, both lenticular and branching, and these commonly show pinch-and-swell texture (Fig. 2a, b). The ore body varies in thickness between 0.33 and 7.3 m (average thickness, 2.1 m). The average grade for the ore body is 2.01 g/t Au and 17.58 g/t Ag. Ore bodies can be divided into gold–silver ore bodies and lead-silver ore bodies. To date, more than 10 ore bodies have been found, including 6 gold–silver ore bodies, 4 lead-silver ore bodies, and numerous other mineralized bodies. The ore is altered-rock type (Fig. 2a, b). The mineralization in the deposit is present as disseminated, veinlet, veined, and brecciated ore. The ore mineralogy consists of pyrite and arsenopyrite (Fig. 2c, d), with minor chalcopyrite, galena, sphalerite, native gold, electrum, native silver, argentite, and pyrargyrite. The gangue consists of quartz, sericite, and calcite. Wall-rock alteration is dominated by silicification (Fig. 2e, f), sericitization

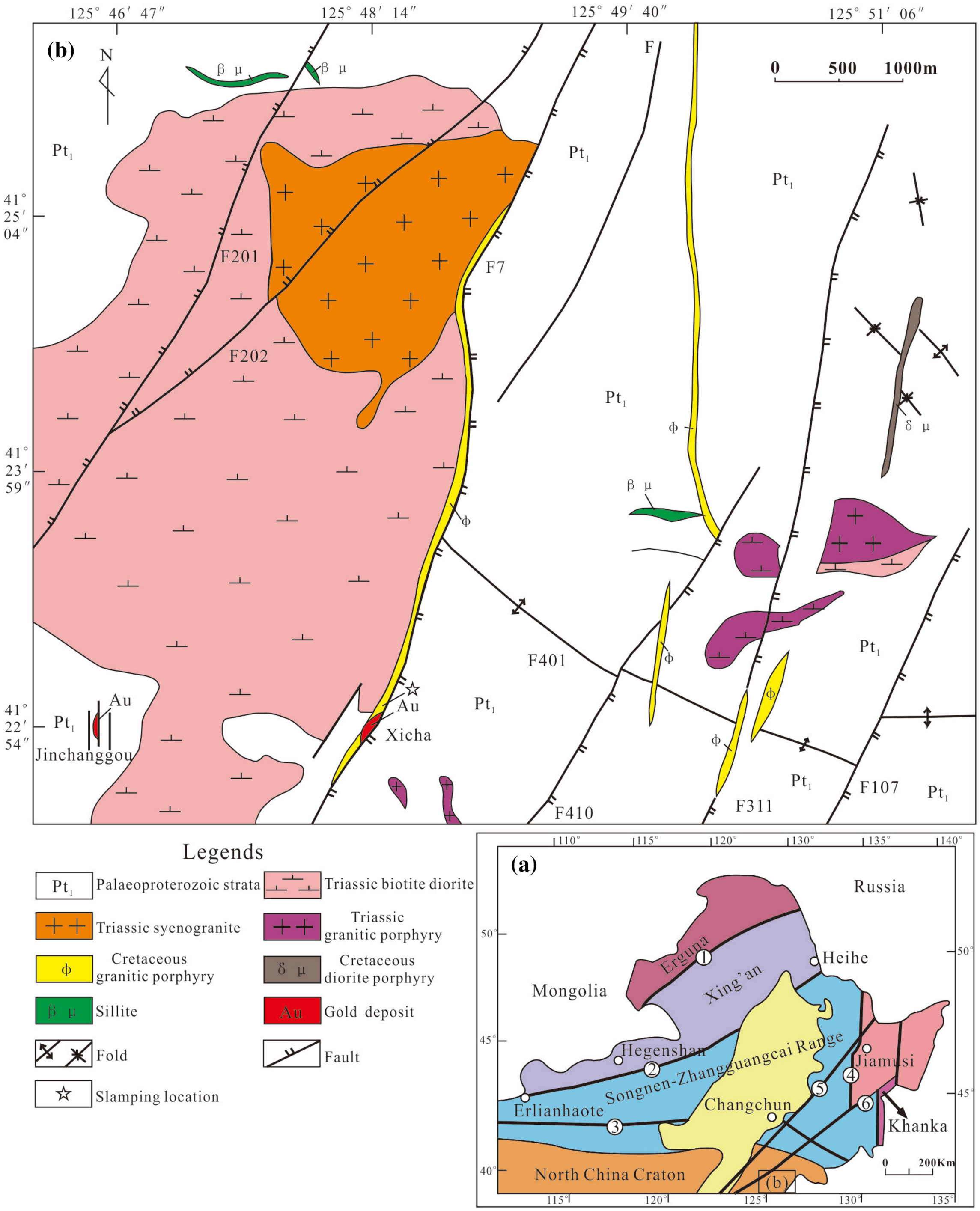

Fig. 1 **a** Tectonic sketch map of NE China, modified after Wu et al. (2011). (1) Xiguitu–Tayuan Fault; (2) Hegenshan–Heihe Fault; (3) Solonker–Xra Moron–ChangchunFault; (4) Mudanjiang Fault; (5) Yitong–Yilan Fault; (6) Dunhua–Mishan Fault. **b** The geological map of Xicha mining area, modified after Guan (2005)2

(Fig. 2e, g), and carbonatization (Fig. 2f), with minor baritization. According to the mineral assemblage, mineralization of the Xicha deposit can be divided into stages of hydrothermal mineralization and supergene mineralization.

The granite porphyry dykes in this study are located along the F7 fault. There is a close spatial relationship between the granite porphyry dykes and gold-bearing veins. The dykes near the ore body are strongly altered and

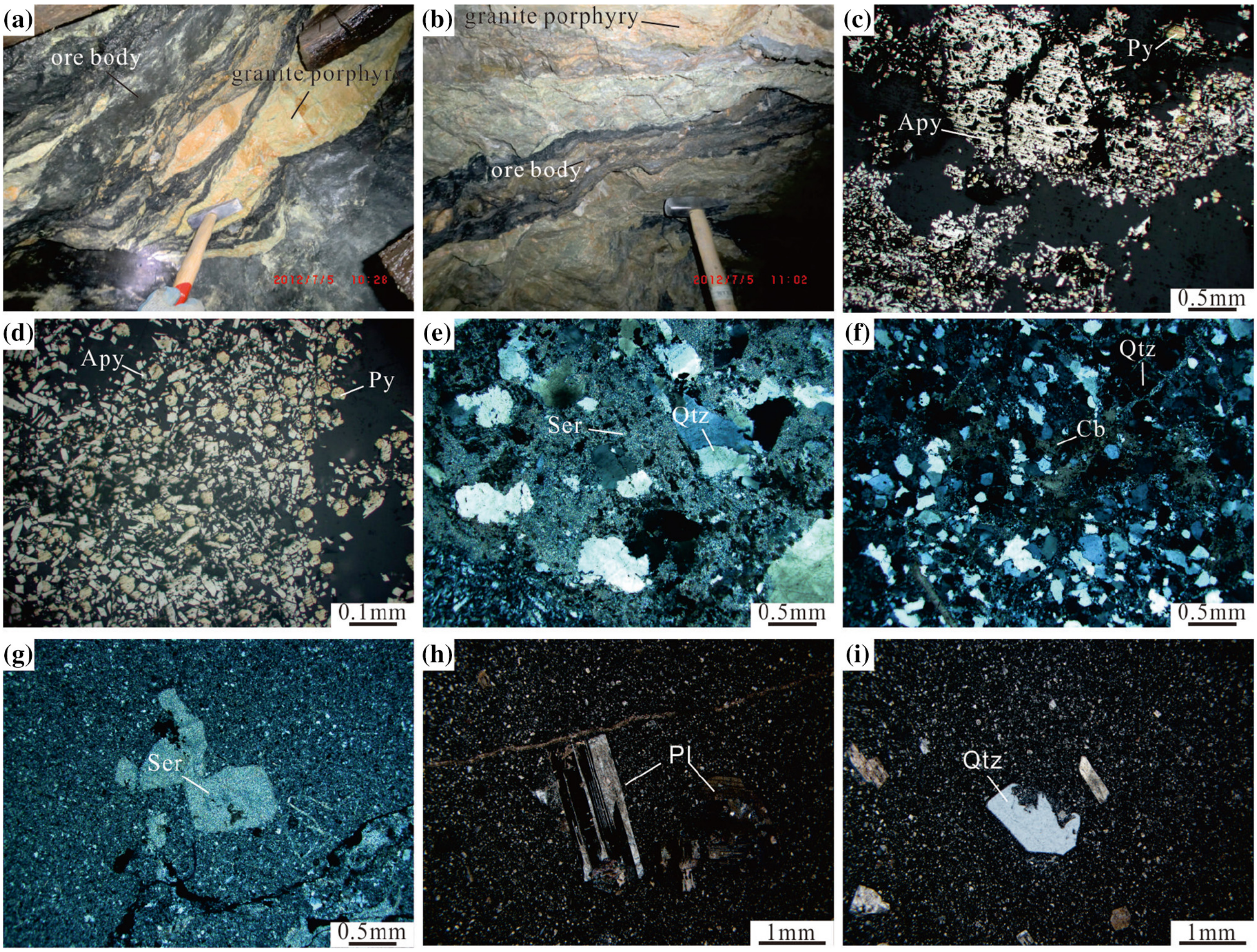

Fig. 2 Photo(micro)graphs of ore body, mineral, alteration and granite pouphyry dykes. **a**, **b** Spatial relationships of ore body and granite porphyry dykes; **c** disseminated arsenopyrite; **d** disseminated arsenopyrite and pyrite; e. quartz and sericite alteration; **f** sericite and carbonate alteration; **g** sericitization granite porphyry; **h** feldspar polysynthetic twins dissolution in phenocrysts; **i** quartz dissolution in phenocrysts

mineralized (Fig. 2g), whereas some dykes located far from the ore body are fresh (Fig. 2i). The dykes and the ore body were possibly coeval or the ore body is slightly younger than the dykes. Samples were collected from the area (41° 23′ 02″ N, 125° 48′ 17″ E) around the mineral deposit for the measurement of zircon U–Pb ages (sample XC-3) and whole-rock geochemical analyses. Samples are fresh or weakly altered, gray in color, and are porphyritic. They also show microscopic crystal structure, felsitic structure in the matrix. Quartz phenocrysts (20% of the total phenocrysts) are anhedral and granular, show weak wavy extinction, and are 0.5–1 mm in size. Plagioclase phenocrysts (80%) are euhedral to subhedral, have polysynthetic twinning, and are 0.2–1 mm in size. The plagioclase has a composition of An = 15–20 according to the Np' ∧ (010) maximum extinction method, indicating oligoclase. The dikes show evidence of weak carbonate alteration. Previously, the dykes were described as albite porphyry (Feng 2000). In the present study, the porphyry has plagioclase and quartz phenocrysts (Fig. 2a, b) and the content of SiO_2 is more than 65 wt%. Therefore, the dykes are defined as granite porphyry.

3 Analytical methods

3.1 Zircon U–Pb dating

Sample XC-N3 was chosen for zircon U–Pb dating of the Xicha granite porphyry. The sample was crushed before zircon were separated using conventional magnetic and heavy liquid methods, with final handpicking of zircon under a binocular microscope for analysis at the Regional Geology Survey, Langfang, Hebei, China. The zircon was mounted in epoxy before being polished to reveal cross-sections for analysis. Prior to analysis, the zircon was imaged under transmitted light and using cathodoluminescence (CL) to reveal internal structures. LA–ICP–MS analysis was undertaken at the State Key Laboratory of Continental Dynamics, Northwest University, Xi'an, China. Helium was used as carrier gas to provide efficient aerosol transport to the ICP and minimize aerosol deposition around the ablation site and within the transport tube (Eggins et al. 1998; Jackson et al. 2004). Argon was used as the make-up gas and was mixed with the carrier gas via a T–connector before entering the ICP. The analysis spots were 32 μm in diameter. U, Th and Pb concentrations were calibrated using ^{29}Si as an internal standard. All measurements were undertaken using an external zircon 91,500 standard with a recommended ^{206}Pb/^{238}U age of 1065.4 ± 0.6 Ma (Wiedenbeck et al. 2004). Analytical procedures used follow those described by Yuan et al. (2004). Raw data were processed using the GLITTER program. Uncertainties of individual analyses are reported with 1σ error; weighted mean ages were calculated at 1σ confidence level. The data were processed using the ISOPLOT (Version 3.0) program (Ludwig 2003).

3.2 Lu–Hf isotope analysis

In-situ zircon Hf isotope analysis was carried out using a NewWave UP213 laser-ablation microprobe, attached to a Neptune multi-collector ICP-MS at the Institute of Mineral Resources, Chinese Academy of Geological Sciences. Instrumental conditions and data acquisition techniques have been comprehensively described by Wu et al. (2006b) and Hou et al. (2007). Lu–Hf isotopic measurements were made on the same zircon grains previously analyzed for U–Pb isotopes, with ablation pits 44 μm in diameter, repetition rates of 8–10 Hz, laser beam energy density of 10 J/cm^2, and an ablation time of 26 s. The analytical procedures were similar to those described in detail by Hou et al. (2007). In order to correct the isobaric interferences of ^{176}Lu and ^{176}Yb on ^{176}Hf, the ratios for ^{176}Lu/^{175}Lu (0.02658) and ^{176}Yb/^{173}Yb (0.796218) were determined (Chu et al. 2002). For instrumental mass bias correction, the Yb isotope ratios were normalized to ^{172}Yb/^{173}Yb = 1.35274 (Chu et al. 2002) and Hf isotope ratios to ^{179}Hf/^{177}Hf = 0.7325, using an exponential law. Zircon GJ1 was used as the reference standard during our routine analyses, with a weighted mean ^{176}Hf/^{177}Hf ratio of 0.282011 ± 24 (2σ, n = 10). This figure is indistinguishable from the weighted mean ^{176}Hf/^{177}Hf ratio of 0.282013 ± 19 (2σ) reported for in situ analysis by Elhlou et al. (2006).

3.3 Whole-rock major and trace element geochemistry

Whole-rock major and trace element concentrations were determined at the Analytical Laboratory of Beijing Research Institute of Uranium Geology. All samples were crushed in a corundum jaw crusher (to 60 mesh) after the removal of weathered surfaces. Then, they were powered in an agate ring mill to less than 200 mesh. Major element concentrations were determined using X-ray fluorescence (XRF) and a PANalytical Axios XRF instrument. Trace element compositions were determined on solutions obtained by sealing and dissolving samples using HF and HNO_3 acids, before conversion into 1 wt% HNO_3 media and addition of an Rh internal standard solution. These solutions were analyzed using inductively coupled plasma–mass spectrometry (ICP–MS) and a PEElan 6000 instrument. The results of international standard BCR-2(basalt), BHVO-1(basalt) and zAGV-1(andesite) show that analytical precision values better than 5 wt% for major elements and better than 10 wt% for trace elements. The detailed sample-digesting procedure for ICP–MS analyses and analytical precision and accuracy for trace elements are the same as description by Liu et al. (2008).

4 Results

4.1 Zircon U–Pb dating

CL images of zircon separated from granite porphyry indicate that they are euhedral to subhedral, are elongate or granular, and contain minor fractures. They generally have concentric magmatic oscillatory zoning (Fig. 3). A total of 15 analyses (Table 1) yielded U concentrations ranging from 62.52 to 740.26 ppm, Th concentrations from 62.52 to 740.26 ppm, and Th/U ratios between 0.11 and 0.78, which are indicative of a magmatic origin (Li et al. 2009a, b). The data plot along or close to the U–Pb Concordia line. Concorde age is 122 ± 1 Ma (MSWD = 1.3, n = 15; Fig. 4a), weighted mean age is 122 ± 1 Ma (MSWD = 0.81, n = 15; Fig. 4b) indicating that the granite porphyry was formed at 122 Ma, during the Early Cretaceous.

4.2 Zircon Lu–Hf isotopes

The zircon Lu–Hf isotopic data are presented in Table 2. The ^{176}Lu/^{177}Hf ratios of 0.001139–0.002385 and $f_{Lu/Hf}$ values of − 0.97 to − 0.93 in the zircon are lower than upper crustal values (^{176}Lu/^{177}Hf = 0.0093, $f_{Lu/Hf-}$ = − 0.72; Vervoort and Patchett 1996). These zircons have $_{176}$Hf/^{177}Hf ratios between 0.282217 and 0.282331,

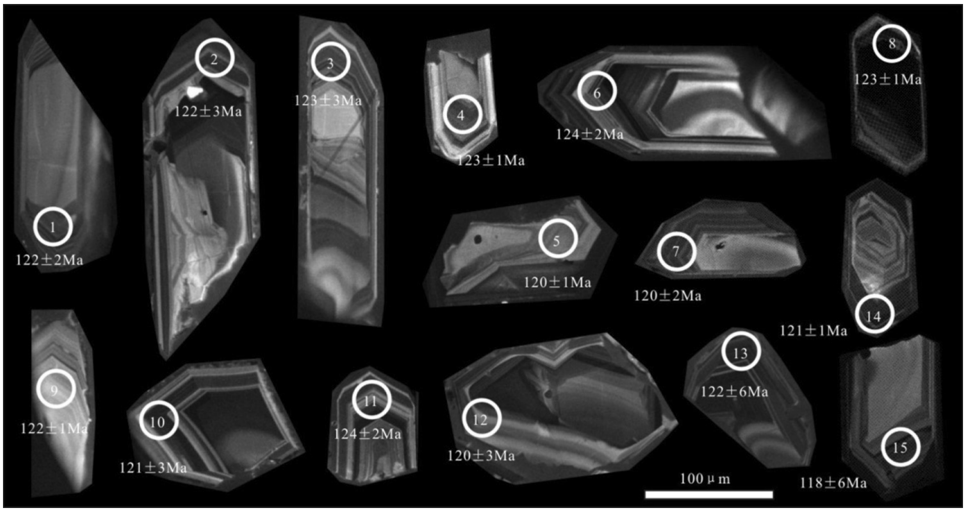

Fig. 3 Cathodoluminescence images of analyzed zircons of Xicha granite porphyry. The small circlets, the Arabic numerals(the number same as Table 1, omission XC-N3-) and the numbers nearby the circlets respectively represent the location of U–Pb in situ erosion, the analytical sequence number and zircon U–Pb age

Table 1 Results of LA–ICP–MS zircon U–Pb dating of Xichа granite porphyry

Analysis	Pb	U	Th	Th/U	$^{207}Pb/^{206}Pb$		$^{207}Pb/^{235}U$		$^{206}Pb/^{238}U$		$^{206}Pb/^{238}U$	
	(ppm)				Ratio	1σ	Ratio	1σ	Ratio	1σ	Age(Ma)	1σ
XC-N3-1	8.9	139.6	372.5	0.37	0.1280	0.0111	0.0191	0.0004	0.0059	0.0003	122	2
XC-N3-2	4.0	125.4	150.5	0.83	0.1300	0.0176	0.0191	0.0006	0.0062	0.0004	122	3
XC-N3-3	31.8	162.9	1460.5	0.11	0.1306	0.0140	0.0193	0.0005	0.0068	0.0008	123	3
XC-N3-4	16.8	153.2	785.0	0.20	0.1307	0.0067	0.0193	0.0002	0.0062	0.0003	123	1
XC-N3-5	20.6	502.3	884.0	0.57	0.1288	0.0054	0.0188	0.0002	0.0055	0.0001	120	1
XC-N3-6	3.1	62.5	128.7	0.49	0.1277	0.0091	0.0194	0.0003	0.0062	0.0002	124	2
XC-N3-7	42.1	740.3	1751.6	0.42	0.1303	0.0042	0.0193	0.0002	0.0062	0.0001	123	1
XC-N3-8	22.9	264.2	914.9	0.29	0.1303	0.0073	0.0188	0.0003	0.0057	0.0002	120	2
XC-N3-9	33.5	214.0	1558.8	0.14	0.1316	0.0051	0.0191	0.0002	0.0072	0.0003	122	1
XC-N3-10	6.9	117.6	281.5	0.42	0.1296	0.0123	0.0189	0.0004	0.0053	0.0003	121	3
XC-N3-11	10.0	230.2	443.5	0.52	0.1304	0.0149	0.0188	0.0005	0.0059	0.0004	120	3
XC-N3-12	15.0	165.7	679.1	0.24	0.1292	0.0098	0.0194	0.0003	0.0072	0.0004	124	2
XC-N3-13	4.2	93.5	120.4	0.78	0.1269	0.0291	0.0191	0.0009	0.0069	0.0007	122	6
XC-N3-14	49.9	615.3	2092.0	0.29	0.1275	0.0049	0.0190	0.0002	0.0059	0.0002	121	1
XC-N3-15	3.7	93.5	120.1	0.78	0.1238	0.0305	0.0185	0.0009	0.0064	0.0007	118	6

εHf(t) values from − 17.1 to − 13.2, and t_{2DM} model ages between 2.01 and 2.26 Ga.

4.3 Geochemistry

4.3.1 Major elements

The whole-rock geochemical data are given in Table 3. The samples are acidic and contain SiO_2 concentrations between 70.64 and 72.31 wt% (average of 71.51 wt%). They contain high Al_2O_3 concentrations (13.99–14.64 wt%), high alkali concentrations (total $K_2O + Na_2O$ between 6.96 and 7.81 wt%), and low concentrations of MgO (0.54–0.83 wt%) and CaO (0.68–1.88 wt%). Their $Mg^{\#}$ values range from 35 to 45. The samples belong to subalkaline granite series (Fig. 5a), have K_2O = 3.85–4.90 wt%, and belong to high-K calc-alkaline series (Fig. 5b), have alumina saturation index (A/CNK) values range from 1.11 to 1.41 and classified to peraluminous (Fig. 5c). They have relatively high K_2O concentrations (3.85–4.90 wt%) and relatively low Na_2O concentrations (2.33–3.21 wt%), yielding K_2O/Na_2O values of 1.24–2.10. The samples contain TiO_2 and $Fe_2O_3^T$

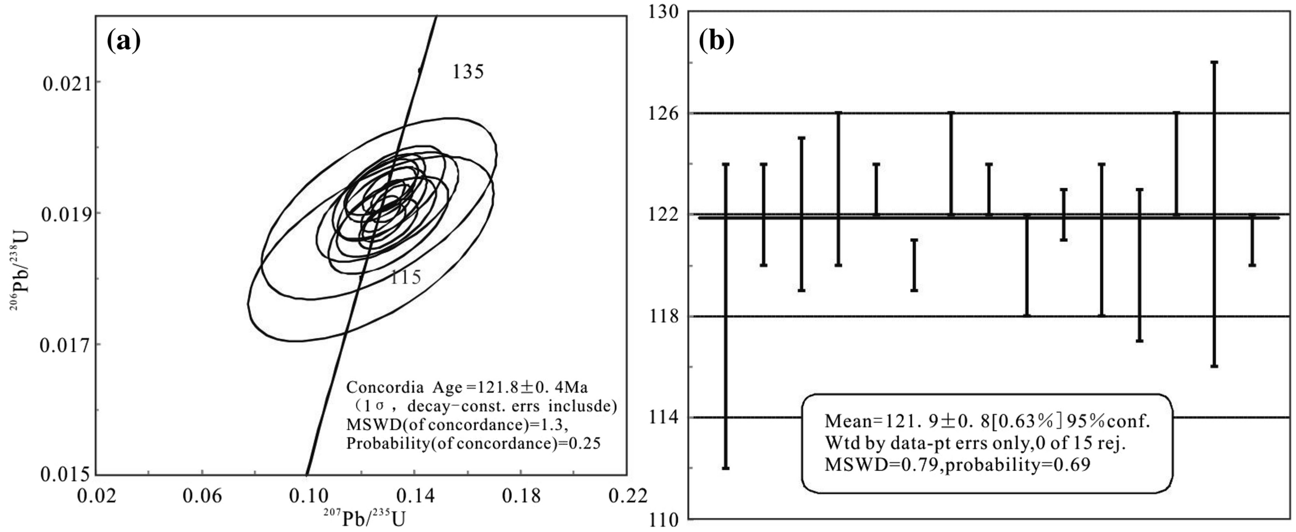

Fig. 4 U–Pb Concordia age (**a**) and weighted average age (**b**) of Xicha granite porphyry

Table 2 Zircon Hf isotopic compositions of Xicha granite porphyry

Analysis	Age/Ma	^{176}Yb/^{177}Hf	^{176}Lu/^{177}Hf	^{176}Hf/^{177}Hf	2σ	(^{176}Hf/^{177}Hf)$_i$	εHf(0)	εHf(t)	T_{DM1}/Ma	T_{DM2}/Ma	$f_{Lu/Hf}$
XC-N3-1	122	0.055010	0.001145	0.282217	0.000025	0.282214	− 19.6	− 17.1	1465	2257	− 0.97
XC-N3-2	122	0.060989	0.001222	0.282246	0.000021	0.282243	− 18.6	− 16.0	1427	2193	− 0.96
XC-N3-3	123	0.086654	0.001759	0.282313	0.000019	0.282309	− 16.2	− 13.7	1352	2045	− 0.95
XC-N3-4	123	0.098652	0.001921	0.282303	0.000019	0.282298	− 16.6	− 14.1	1373	2069	− 0.94
XC-N3-5	120	0.054968	0.001139	0.282269	0.000020	0.282266	− 17.8	− 15.3	1392	2143	− 0.97
XC-N3-6	124	0.094741	0.001906	0.282289	0.000020	0.282284	− 17.1	− 14.5	1393	2100	− 0.94
XC-N3-7	123	0.077953	0.001565	0.282244	0.000019	0.282241	− 18.7	− 16.1	1443	2198	− 0.95
XC-N3-8	120	0.124978	0.002385	0.282331	0.000020	0.282325	− 15.6	− 13.2	1350	2010	− 0.93
XC-N3-9	122	0.082359	0.001568	0.282321	0.000018	0.282317	− 16.0	− 13.4	1335	2028	− 0.95
XC-N3-10	121	0.056989	0.001188	0.282267	0.000019	0.282264	− 17.9	− 15.3	1397	2147	− 0.96
XC-N3-11	120	0.106355	0.002072	0.282289	0.000018	0.282284	− 17.1	− 14.6	1399	2103	− 0.94
XC-N3-12	124	0.106597	0.002098	0.282297	0.000018	0.282292	− 16.8	− 14.3	1388	2082	− 0.94
XC-N3-13	122	0.103576	0.002062	0.282303	0.000017	0.282298	− 16.6	− 14.1	1378	2070	− 0.94
XC-N3-14	121	0.109042	0.002168	0.282248	0.000023	0.282243	− 18.5	− 16.1	1461	2193	− 0.93
XC-N3-15	118	0.099584	0.001996	0.282235	0.000019	0.282230	− 19.0	− 16.6	1473	2224	− 0.94

$\varepsilon Hf(0) = [(^{176}Hf/^{177}Hf)_S/(^{176}Hf/^{177}Hf)_{CHUR,0} - 1] \times 10000$; $\varepsilon Hf(t) = \{[(^{176}Hf/^{177}Hf)_S\text{-}(^{176}Lu/^{177}Hf)_S \times (e^{\lambda t} - 1)]/[(^{176}Hf/^{177}Hf)_{CHUR,0}\text{-}(^{176}Lu/^{177}Hf)_{CHUR} \times (e^{\lambda t} - 1)] - 1\} \times 10000$; $T_{Hf1} = 1/\lambda \times \{1 + [(^{176}Hf/^{177}Hf)_S\text{-}(^{176}Hf/^{177}Hf)_{DM})/(^{176}Lu/^{177}Hf)_S\text{-}(^{176}Lu/^{177}Hf)_{DM}]\}$; $T_{Hf2\text{-}} = T_{Hf1}\text{-}(T_{Hf1}\text{-}t)[(f_{CC}\text{-}f_S)/(f_{CC}\text{-}f_{DM})]$; $f_{Lu/Hf} = (^{176}Lu/^{177}Hf)_S/(^{176}Lu/^{177}Hf)_{CHUR\text{-}1}$; $(^{176}Lu/^{177}Hf)_S$ and $(^{176}Hf/^{177}Hf)_S$ are sample measurements; $(^{176}Lu/^{177}Hf)_{CHUR} = 0.0322$,$(^{176}Hf/^{177}Hf)_{CHUR,0} = 0.282772$; $(^{176}Lu/^{177}Hf)_{DM} = 0.0384$,$(^{176}Hf/^{177}Hf)_{DM} = 0.28325$; f_{CC}, f_S and f_{DM} stands for $f_{Lu/Hf}$ of crust, samples and depleted mantle respectively; t is the formation time of the samples; $\lambda = 1.867 \times 10^{-11}$ a^{-1}

concentrations of 0.18–0.22 and 1.95–2.44 wt%, respectively.

4.3.2 Trace elements

The trace element compositions of the samples are presented in Table 3. Total rare earth element (ΣREE) concentrations range between 75.02 and 94.35 ppm, with an average of 84.43 ppm. They have chondrite-normalized REE patterns that decrease to the right (Fig. 6a), and they are characterized by clear fractionation of the REEs, with LREE enrichments, LREE/HREE ratios of 9.93–11.97, and $(La/Yb)_N$ values of 11.08–15.16. The samples also show weak negative Eu anomalies (Eu/Eu* = 0.69–0.95) and have low concentrations of HREEs, indicating the granite porphyry was formed by partial melting with plagioclase-in-melt.

Table 3 Major (wt%) and trace element (ppm) data for the Xicha granite porphyry

Sample	JCG-3-1	JCG-3-2	JCG-3-3	JCG-3-4	JCG-3-5	JCG-3-6	JCG-3-7	JCG-3-8	JCG-3-9
SiO_2	71.79	71.23	71.55	71.24	70.64	71.66	71.42	72.31	71.72
TiO_2	0.18	0.18	0.19	0.19	0.22	0.19	0.19	0.18	0.19
Al_2O_3	14.35	14.41	14.38	14.57	14.16	14.55	13.99	14.64	14.34
$Fe_2O_3^T$	2.08	2.00	1.95	2.06	2.44	2.09	1.97	2.02	1.98
MnO	0.10	0.09	0.08	0.09	0.12	0.10	0.09	0.06	0.09
MgO	0.57	0.58	0.57	0.56	0.69	0.54	0.83	0.69	0.6
CaO	1.29	1.51	1.26	1.18	1.88	0.98	1.75	0.68	1.36
Na_2O	3.21	3.17	3.10	3.11	3.00	3.02	3.11	2.33	3.18
K_2O	4.09	4.20	4.44	4.47	4.03	4.79	3.85	4.90	4.11
P_2O_5	0.06	0.06	0.05	0.06	0.07	0.06	0.05	0.06	0.06
LOI	2.21	2.50	2.37	2.43	2.68	1.95	2.69	2.08	2.34
Total	99.92	99.92	99.94	99.96	99.93	99.93	99.93	99.95	99.96
K_2O/Na_2O	1.27	1.32	1.43	1.44	1.34	1.59	1.24	2.10	1.29
ALK	7.30	7.37	7.54	7.58	7.03	7.81	6.96	7.23	7.29
A/NK	1.48	1.47	1.45	1.46	1.52	1.43	1.51	1.60	1.48
A/CNK	1.19	1.15	1.18	1.20	1.11	1.22	1.12	1.41	1.18
La	17.6	18.2	18.3	19.9	21.1	22.2	20.4	19.2	20.1
Ce	31.4	32.4	33.8	35.4	41.1	38.3	37.5	36.4	37.1
Pr	3.55	3.76	3.93	3.94	4.56	4.12	4.16	3.96	4.18
Nd	13.2	14.4	13.6	14.5	16.2	160	15.1	13.6	14.7
Sm	2.23	2.44	2.39	2.66	2.99	2.90	2.91	2.35	2.6
Eu	0.61	0.71	0.52	0.70	0.74	0.66	0.73	0.56	0.64
Gd	1.86	2.02	2.12	2.01	2.41	2.20	2.17	2.10	2.04
Tb	0.31	0.35	0.34	0.36	0.39	0.36	0.37	0.34	0.33
Dy	1.78	2.05	1.82	1.95	1.98	1.83	2.08	1.72	1.79
Ho	0.33	0.36	0.35	0.35	0.36	0.34	0.35	0.32	0.33
Er	0.99	1.10	0.97	0.96	1.07	1.00	1.08	0.94	0.98
Tm	0.13	0.16	0.14	0.15	0.15	0.16	0.15	0.15	0.13
Yb	0.89	1.04	0.95	0.97	1.03	0.99	0.99	0.96	0.90
Lu	0.14	0.16	0.15	0.16	0.17	0.15	0.15	0.16	0.15
ΣREE	75.02	79.14	79.38	84.01	94.25	91.21	88.14	82.76	85.97
LREE/HREE	10.66	9.93	10.61	11.15	11.47	11.97	11.01	11.37	11.92
$(La/Yb)_N$	13.36	11.8	12.95	13.8	13.81	15.16	13.96	13.55	14.99
δEu	0.88	0.95	0.69	0.89	0.81	0.77	0.85	0.76	0.82
Rb	132	143	143	135	130	143	129	168	132
Sr	259	288	248	249	281	242	277	193	252
Ba	986	1044	1046	1030	993	1090	948	844	933
Y	10.2	11.7	10.5	11.3	11.7	10.5	11.1	10.4	10.4
Nb	15.4	17.1	14.6	17.0	16.3	16.8	16.3	16.7	15.3
Ta	1.16	1.30	1.17	1.26	1.18	1.24	1.20	1.23	1.23
Zr	75.4	79.5	79.2	79.7	79.9	76.5	76.1	79.3	75.9
Hf	2.99	2.99	2.87	3.03	3.23	3.24	2.85	3.28	3.12
Th	5.85	6.26	5.65	6.08	6.55	6.36	6.05	5.92	6.17
U	1.93	2.12	1.85	2.00	1.86	2.31	1.92	1.90	1.92
Ga	18.3	19.8	17.8	18.7	19.2	18.7	18.7	19.2	18.8
Nb/Ta	13.28	13.15	12.48	13.49	13.81	13.55	13.58	13.58	12.44
Rb/Sr	0.51	0.50	0.58	0.54	0.46	0.59	0.47	0.87	0.52
Rb/Nb	8.57	8.36	9.79	7.94	7.98	8.51	7.91	10.06	8.63

Table 3 continued

Sample	JCG-3-1	JCG-3-2	JCG-3-3	JCG-3-4	JCG-3-5	JCG-3-6	JCG-3-7	JCG-3-8	JCG-3-9
Nb/La	0.88	0.94	0.8	0.85	0.77	0.76	0.8	0.87	0.76

ALK = $K_2O + N_2O$; A/NK = mol $[Al_2O_3/(Na_2O + K_2O)]$; A/CNK = mol $[Al_2O_3/(CaO + Na_2O + K_2O)]$; LREE = La + Ce + Pr + Nd + Sm + Eu; HREE = Gd + Tb + Dy + Ho + Er + Tm + Yb + Lu; $\sum$REE = LREE + HREE; $(La/Yb)_N = (La/0.687)/(Yb/0.493)$; δEu = (Eu)cn/[(Gd)cn + (Sm)cn]/2

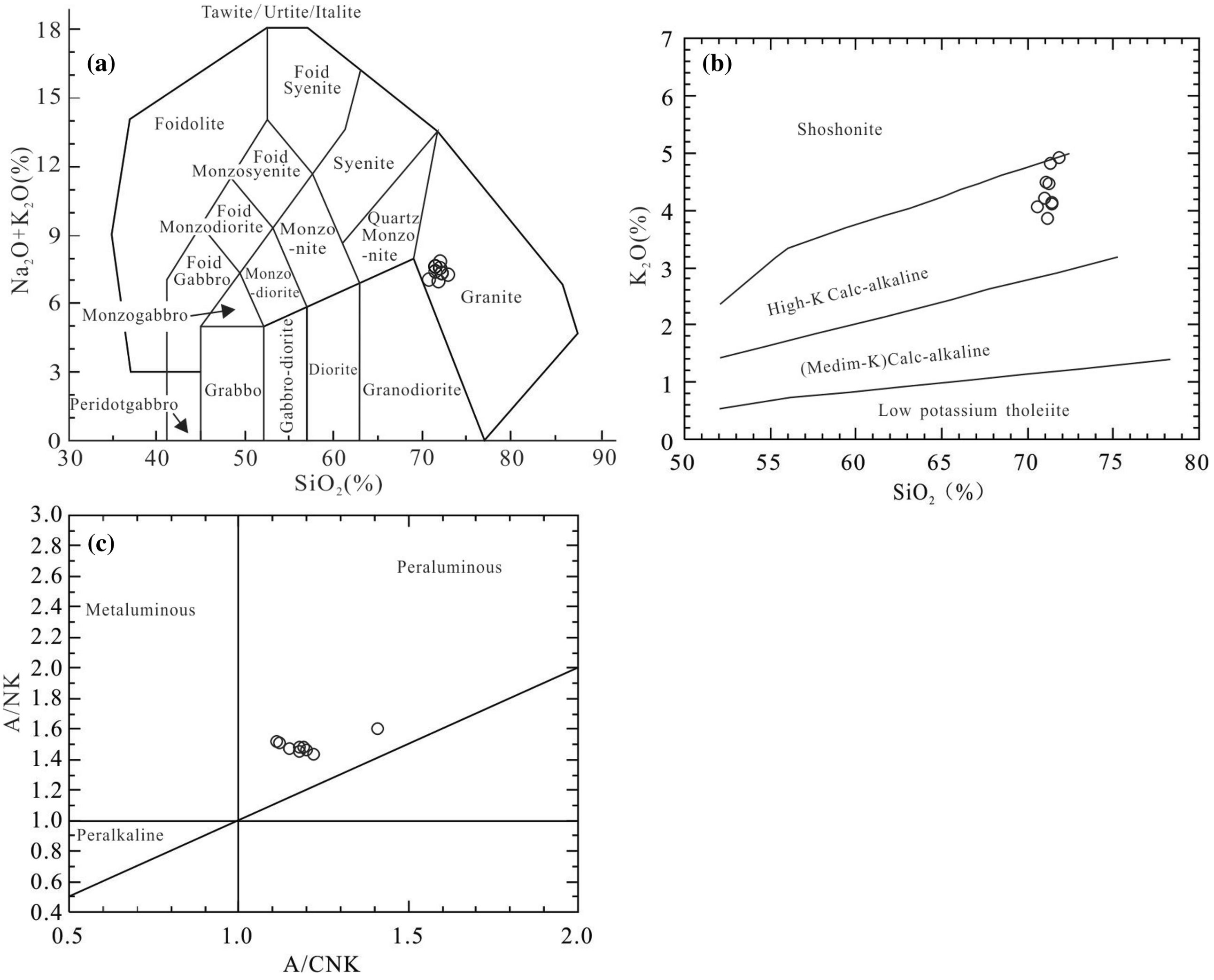

Fig. 5 TAS diagram [**a** after Irvine and Bangmi (1971)], SiO_2–K_2O diagram [**b** after Peccerillo and Taylor (1976)] and A/CNK–A/NK diagram [**c** after Maniar and Piccoli (1989)] for Xicha granite porphyry

The granite porphyry samples have uniform primitive-mantle-normalized trace element patterns (Fig. 6b), which demonstrate that large ion lithophile elements (LILEs) and incompatible elements (e.g., K, Rb, Sr, Th, and U) are enriched, whereas the high field strength elements (HFSEs) Ti and P are depleted. These samples have variable element ratios, such as Rb/Sr (0.46–0.87), Nb/Ta (12.44–13.81), Rb/Nb (7.91–10.06), and Nb/La (0.76–0.94).

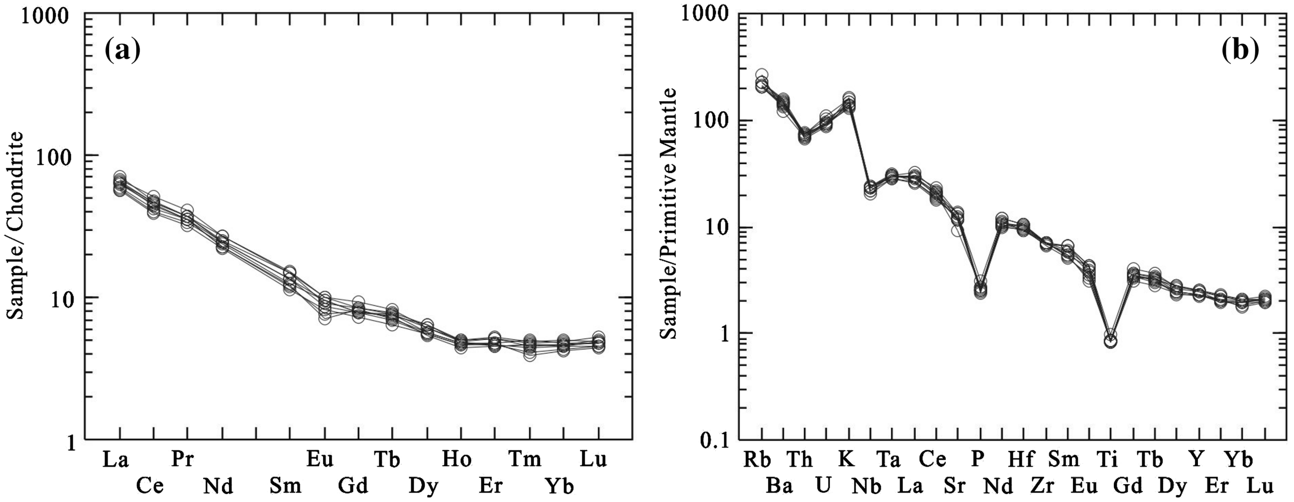

Fig. 6 Chondrite-normalized REE patterns (**a**) and primitive mantle-normalized trace element patterns (**b**) for the Xicha granite porphyry [chondrite REE values from Boynton (1984); primitive mantle values from Sun and Mcdonough (1989)]

5 Discussion

5.1 Magma sourcing and petrogenesis

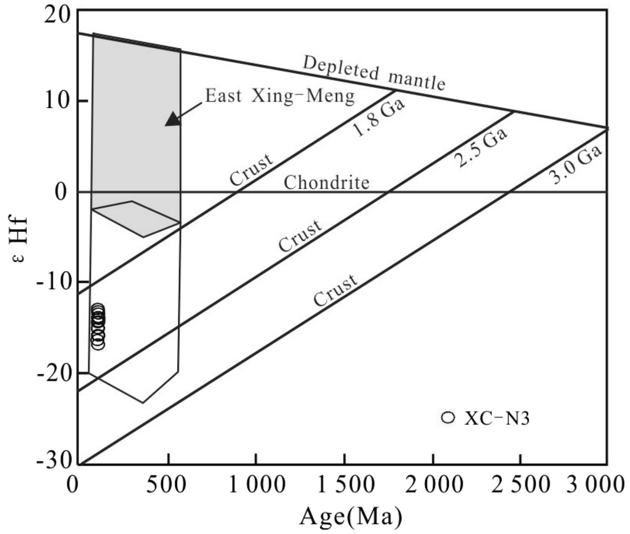

Fig. 7 εHf–t diagram of Xicha granite porphyry [after Yang et al. (2006)]

The results of major element geochemistry indicate that the granite porphyry dykes contain high concentrations of SiO_2, Al_2O_3, and alkali elements, and low concentrations of CaO, MgO, and Fe_2O_3. The K_2O/Na_2O ratios are greater than 1 and the alumina saturation index (A/CNK) values are greater than 1.1. The average content of Na_2O is less than 3.2. Corundum containing (1.66–4.51%) more than 1% is found in CIPW standard minerals. When SiO_2 content is 66%, CaO content is less than 3.7%. These features are all characteristic of S-type granites (Sang and Ma 2012). The $Mg^{\#}$ value of a rock reflects whether the source magma that formed the rock was derived from crustal material alone or from crustal material that has been contaminated by mantle material (Smithies and Champion 2000). The low $Mg^{\#}$ (35–45) values of the samples analyzed from this study do not support any interaction between the crust and the mantle materials. The enrichment in LILEs and depletion in HFSEs also reveal that these rocks formed from magmas derived from the melting of crustal material (Taylor and McLennan 1985; Hofmann 1988). The REE patterns decrease to the right, as LREEs are enriched and HREEs are depleted. This indicates the presence of residual garnet in the source of the magmas that formed the porphyry granite dykes and suggests a crustal thickness greater than that of average crust. The granite porphyry has Nb/Ta ratios of 12.44–13.81, which are consistent with the Nb/Ta ratios of magmas generated by the melting of crustal material (i.e., 11–12; Green 1995). In addition, they have Rb/Sr ratios of 0.46–0.87 and Rb/Nb ratios of 7.97–10.06, which are similar to the ratios expected for crustal material (0.32 and 4.5, respectively; Taylor and McLennan 1985). The samples have negative εHf(t) values, indicating a crustal origin, and they plot along the crustal line on a εHf(t)-t diagram (Fig. 7). The negative εHf(t) values and the t_{2DM} model ages of 2.01–2.26 Ga indicate the granite porphyry formed from magmas derived from partial melting of Paleoproterozoic lower crustal material. Sylvester (1998) combined experimental studies with a statistical analysis of the components of typical orogenic granites around the world and suggested that variations in the Al_2O_3/TiO_2 ratios of strongly peraluminous granites with SiO_2 concentrations of 67–77 wt% are indicative of partial melting temperatures. For example, samples with Al_2O_3/TiO_2 ratios of < 100

must have formed from magmas generated by partial melting at temperatures of > 875 °C. The samples analyzed during this study have Al_2O_3/TiO_2 ratios range from 64.4 to 81.3, indicating The porphyry formation temperature is greater than 875 °C. Sr content is from 193 to 288, Yb content is from 0.89 to 1.04, indicating the samples belong to Himalaya-type granite (Zhang et al. 2006) formed at a pressure of 0.8–1.5 GPa corresponding depth of 45–50 km (Zhang et al. 2011).

5.2 Age of granite porphyry formation

To our knowledge, the granite porphyry dykes have not previously been dated. Results of the present study indicate that the zircon has concentric magmatic oscillatory zoning, high concentrations of U (120.38–2090.03 ppm) and Th (62.52–740.26 ppm), and high Th/U ratios of 0.11–0.78, which are all characteristics of a magmatic origin. The weighted age shows that the granite porphyry was emplaced at 122 Ma. Studies have shown that Early Cretaceous magmatic events are widespread in southern Jilin. For example, the Shanglushuiqiao granite was emplaced at 118 ± 2 Ma (Qin et al. 2012), the Chibosong gabbro was emplaced at 134 ± 7 Ma (Pei et al. 2005), the Sankeyushu Group trachyte was formed at 118 Ma (Sui and Chen 2012), and diorite dykes in this study area were emplaced at 126 ± 1 Ma. Early Cretaceous magmatic events are also widely distributed in eastern China, including the Jiaodong Peninsula, the Liaodong Peninsula, Yanshan and western Liaoning, western Shandong, and the Taihang Mountains of North China (Guo et al. 2004; Wu et al. 2005a, b), as well as in the eastern and southern Da-Hinggan Mountains in northeast China (Guo et al. 2004; Qin et al. 2012). Most of the Early Cretaceous granites in eastern China are classified as A-type granites.

5.3 Early cretaceous lithospheric thinning and mineralization in the Xicha deposit

Analyses of mantle xenoliths from basalts show that the lithosphere in Eastern China underwent a thinning of at least 100 km during the Mesozoic and that the thickness was only 80–100 km in the Cenozoic (Fan and Hooper 1989; Chi 1988). The lithosphere changed from old, low-density, cold, and isotopically enriched to young, high-density, hot, and isotopically depleted (Lu et al. 1991). There are two main mechanisms of lithospheric thinning: delamination (Wu et al. 2006a) and thermal erosion (Zheng et al. 2006, 2007). To identify the timing of lithospheric thinning, we recently proposed the following indicators: (1) widespread intense magmatism; (2) a change in mantle magma from asthenospheric to lithospheric; (3) the generation of metamorphic core complexes and extensional basins; and (4) a change in the elevation of terrain from high to low (Wu et al. 2008). Wu et al. (2005b, 2006a) suggested that large-scale magmatic activity in the North China Craton began in the Middle Jurassic, in two stages at 180–155 and 135–115 Ma. During the earlier stage, magmatism was mainly distributed along the margins of North China, with none inland, and was related to subduction of the ancient Pacific Ocean plate. During the later stage, magmatism was widely distributed throughout North China, and the coexistence of different sources and depths suggests that significant lithospheric thinning occurred during the Early Cretaceous.

Metamorphic core complexes, faulted basins, detachment faults, syntectonic magmatic rocks, and extensional tectonics are widely developed in the Early Cretaceous of North China, and previous studies have indicated that these features are the surface response to lithospheric thinning. Liu et al. (2006) analyzed the Yagan and Hohhot metamorphic core complex in the north of North China, the Waziyu and south Liaoning metamorphic core complexes in the east of North China, and the Xiaoqinling and Yunmengshan core complexes in the south, and reported an average stretching lineation direction of 130°–310°, indicating that the lineations formed in the same stress field; the age of formation was 130–120 Ma. Zhu et al. (2008) studied an Early Cretaceous extensional basin in North China and proposed that lithospheric delamination was the main mechanism of lithospheric thinning. Lin et al. (2011) studied a metamorphic core complex, syntectonic granites, and low-angle detachment faults on the Liaodong Peninsula, and demonstrated that they all have an NW–SE direction at the regional scale and formed between 130 and 120 Ma. The studies above show that large-scale lithospheric thinning occurred in the Early Cretaceous in North China.

Based on the present work and previous studies, the following model is proposed for the mineralization of the Xicha gold–(silver) deposit. During the Early Cretaceous, large-scale lithospheric thinning occurred in North China. The asthenosphere rose upward, heating the lower crust prompting partial melting of various crustal components. Mineral-enriched mantle fluids and magmas derived from the melting of the various components intruded simultaneously and syntectonically. The ore-forming fluid, enriched in CO_2 and other volatile components, extracted Au, Ag, and other ore-forming elements from ancient basement rocks and rose along NE–SW trending faults. When the fluids reached the shallow crust, changes in temperature and pressure, as well as mixing with meteoric waters, led to the formation of the mineralized veins and the alteration of rocks and dykes.

6 Conclusions

1. Granite porphyry dykes and gold-bearing veins in the Xicha gold deposit are formed at nearly the same time during the Early Cretaceous (122 ± 1 Ma) under the same tectonic background.
2. The granite porphyry dykes formed from magmas that were derived from the partial melting of Paleoproterozoic lower-crustal material.
3. Xicha gold–(silver) deposit and granite porphyry dykes in Northeast China represent the surface response to lithospheric thinning.

Acknowledgements The current research was supported by the Undergraduate Institutions Basic Scientific Research Foundation of Heilongjiang Province (Hkdcx201805), the Natural Science Foundation of Heilongjiang Province, China (QC2017035) and the National Nature Science of Foundation of China (41272093). The authors thank Professor Liu Xiaoming of State Key Laboratory of Continental Dynamics, Northwest University, Xi'an, China, for helping in LA–ICP–MS dating. The authors would like to thank ALS Chemex Co., Ltd., Guangzhou, China, for helping in major and trace element analyses. The authors also give their thanks to Institute of Mineral Resources, Chinese Academy of Geological Sciences for assisting in the Hf isotope analyses.

References

Boynton WV (1984) Cosmochemistry of the rare earth elements: meteorite studies. In: Henderson P (ed) Rare earth elements geochemistry. Elsevier, Amsterdam, pp 63–144

Chi JS (1988) Study on Cenozoic basalts and upper mantle Eastern China. China University of Geosciences Press, Wuhan, 258p **(in Chinese)**

Chu NC, Taylor RN, Chavagnac V, Nesbitt RW, Boella RM, Milton JA, German CR, Bayon G, Burton K (2002) Hf isotope ratio analysis using multi-collector inductively coupled plasma mass spectrometry: an evaluation of isobaric interference corrections. J Anal Sci Technol 17:1567–1574

Deng SH, Wan CB, Yang JG (2009) Discovery of a Late Permian Angara-Cathaysia mixed flora from Acheng of Heilongjiang, China, with discussions on the closure of the Paleoasian Ocean. Sci China, Ser D Earth Sci 52:1746–1755 **(in Chinese with English abstract)**

Eggins SM, Kinsley LPJ, Shelley JMM (1998) Deposition elemental fractionation processes during atmospheric pressure laser sampling for analysis by ICP–MS. Appl Surf Sci 127–129:278–286

Elhlou S, Belousova E, Griffin WL (2006) Trace element and isotopic composition of GJ-red zircon standard by laser ablation. Geochim Cosmochim Acta 70:A158

Fan QC, Hooper PR (1989) The mineral chemistry of ultramafic xenoliths of eastern China: implications for upper mantle composition and the paleogeotherms. J Petrol 30:1117–1158

Feng SZ (2000) The geological character and metallogenic mechanism of the Xicha Jinchanggou gold deposit. Gold Sci Technol 8:29–35 **(in Chinese with English abstract)**

Green TH (1995) Significance of Nb/Ta as an indicator of geochemical processes in the crust–mantle system. Chem Geol 120:347–359

Guan J (2005) Study on metallogenetic law of precious and non ferrous deposits in the southeast part of Jilin Province. Jilin University College of Earth Science, Changchun **(in Chinese with English abstract)**

Guo CL, Wu FY, Yang JH, Lin JQ, Sun DY (2004) The extensional setting of the Early Cretaceous magmatism in eastern China: example from the Yinmawanshan pluton in southern Liaodong Peninsula. Acta Petrol Sinica 20:1193–1204 **(in Chinese with English abstract)**

Guo F, Fan WM, Miao LC, Zhao L (2009) Early Paleozoic subduction of the Paleo-Asian Ocean: geochronological and geochemical evidence from the Dashizhai basalts, Inner Mongolia. Sci China 39:569–579 **(in Chinese with English abstract)**

Hofmann AW (1988) Chemical differentiation of the earth: the relationship between mantle, continental crust, and oceanic crust. Earth Planet Sci Lett 90:297–314

Hou KJ, Li YH, Zou TR, Qu XM, Shi YR, Xie GQ (2007) Laser ablation-MC-ICP-MS technique for Hf isotope microanalysis of zircon and its geological applications. Acta Petrol Sinica 23:2595–2640 **(in Chinese with English abstract)**

Irvine TH, Bangmi WRA (1971) A guide to the chemical classification of the common volcanic rocks. Can J Earth Sci 8:523–548

Jackson SE, Pearson NJ, Griffin WL, Belousova EA (2004) The application of laser ablation-inductively coupled plasma–mass spectrometry to in situ U–Pb zircon geochronology. Chem Geol 211(1):47–69

Li JW, Vasconcelos PM, Zhang J (2003) ^{40}Ar/^{39}Ar constraints on a temporal link between gold mineralization, magmatism, and continental margin transtension in the Jiaodong gold province. J Geol 111:741–751

Li BL, Chen GJ, Song ZW (2004) Discussion on minerogenetic epoch of the gold deposit in Jiapigou of Jilin Province. Glob Geol 23:354–359 **(in Chinese with English abstract)**

Li HK, Gen JZ, Hao S, Zhang YQ, Li HM (2009a) Research on the dating zircon U–Pb age by LA-MC-ICPMS. Bull Mineral Petrol Geochem 28:77 **(in Chinese with English abstract)**

Li PW, Gao R, Guan Y, Li QS (2009b) The closure time of the Paleo-Asian Ocean and the Paleo-Tethys Ocean: implication for the tectonic cause of the end-Permian mass extinction. J Jilin Univ (Earth Sci Ed) 39:521–527 **(in Chinese with English abstract)**

Lin W, Wang QC, Wang J, Wang F, Zhe Y, Chen K (2011) Late Mesozoic extensional tectonics of the Liaodong Peninsula massif: response of crust to continental lithosphere destruction of the North China Craton. Sci China Earth Sci 54:843–857 **(in Chinese with English abstract)**

Liu JL, Guan HM, Ji M, Hu L (2006) Late Mesozoic metamorphic core complex and its constraints on the mechanism of lithospheric thinning in North China. Prog Nat Sci 16:21–27 **(in Chinese)**

Liu YS, Zong KQ, Kelemen PB, Gao S (2008) Geochemistry and magmatic history of eclogites and ultramafic rocks from the Chinese continental scientific drill hole: subduction and ultrahigh-pressure metamorphism of lower crustal cumulates. Chem Geol 247(1–2):133–153

Lu FX, Han ZG, Zheng JP, Ren YX (1991) Characteristics of Paleozoic mantle-lithosphere in Fuxian, Liaoning Province. Geol Sci Technol Inf 10:2–20 **(in Chinese with English abstract)**

Lu XP, Wu FY, Zhao CB, Zhang YB (2003) Relationship between zircon U-Pb age of Indosinian granites in Tonghua district and Dabie-Sulu ultra high pressure orogenic belt. Chin Sci Bull 48:843–849 **(in Chinese)**

Lu XP, Wu FY, Zhang YB, Zhao CB, Guo CL (2004) Emplacement age and tectonic setting of the Paleoproterozoic Liaoji granites in Tonghua area, southern Jilin province. Acta Petrol Sinica 20:381–392 **(in Chinese with English abstract)**

Ludwig KR (2003) User's manual for Isoplot 3.00: a geochronological toolkit for Microsoft Excel. Berkeley Geochronology Center Special Publication, 4, 70

Luo ZK, Guan K, Miao LC (2002) Dating of the dykes and altered sericite in Jiapigou gold ore belt, Jilin province and its gold ore formation age. Geoscience 16:19–25 **(in Chinese with English abstract)**

Maniar PD, Piccoli PM (1989) Tectonic discrimination of granitoids. Geol Soc Am Bull 101:635–643

Mao JW, Zhang ZH, Yu JJ, Wang YT, Nu BG (2003) Mesozoic large-scale mineralization geodynamic background in North China and adjacent areas: implication from precise age measurement of metal deposits. Sci China Ser D 33:289–299 **(in Chinese)**

Mao JW, Xie GQ, Zhang ZH, Li XF, Wang YT, Zhang CQ, Li YF (2005) Mesozoic large-scale metallogenic pulses in North China and corresponding geodynamic setting. Acta Petrol Sinica 21:169–188 **(in Chinese with English abstract)**

Peccerillo A, Taylor AR (1976) Geochemistry of Eocene calc-alkaline volcanic rocks from the Kastamonu area, northern Turkey. Contrib Miner Petrol 58:63–81

Pei FP, Xu WL, Yu Y, Zhao GQ, Yang DB (2005) Petrogenesis of the Late Triassic Mayihe pluton in southern Jilin province: evidence from zircon U-Pb geochronology and geochemistry. J Jilin Univ (Earth Sci Ed) 38:351–362 **(in Chinese with English abstract)**

Qin Y, Liang YH, Hu ZC, Feng J, Song ZT, Li M (2012) Geochemical characteristics and tectonic significance of the Shanglüshuiqiao aluminous A-type granites intrusive in the Ji'an area, Jilin province. J Jilin Univ (Earth Sci Ed) 42:1076–1083 **(in Chinese with English abstract)**

Sang LK, Ma CQ (2012) Petrology. Geological Press, pp 1–342 **(in Chinese)**

Smithies RH, Champion DC (2000) The Archaean high-Mg diorite suite: links to tonalite–trondhjemite–granodiorite magmatism and implications for Early Archaean crustal growth. J Petrol 41:1653–1671

Sui ZM, Chen YJ (2012) Petrogenesis of volcanic rocks from Sankeyushu formation in Southern Jilin: evidences from zircon U-Pb ages and Hf isotopes. Geoscience 26:627–634 **(in Chinese with English abstract)**

Sun SS, Mcdonough WF (1989) Chemical and isotopic systematics of oceanic basalts: implications for mantle composition and processes. in magmatism in ocean basins. Geol Soc Lond Geol Soc Spec Publ 42:313–345

Sun DY, Wu FY, Gao S, Lu XP (2005) Confirmation of two episodes of A-type granite emplacement during Late Triassic and Early Jurassic in the central Jilin Province, and their constraints on the structural pattern of eastern Jilin-Heilongjiang area, China. Earth Sci Front 12:263–275 **(in Chinese with English abstract)**

Sylvester PJ (1998) Post-collisional strongly peraluminous granites. Lithos 45:29–44

Taylor SR, McLennan SM (1985) The continental crust: its composition and evolution. Blackwell Scientific Publication, Oxford, pp 1–132

Vervoort JD, Patchett PJ (1996) Behavior of hafnium and neodymium isotopes in the crust: constraints from Precambrian crustally derived granites. Geochim Cosmochim Acta 60:3717–3733

Wang J, Li BL, Sun FY (2016) Age, petrogenesis and Tectonic Implication of Late Triassic Granitoids in Jinchanggou Orefield, Southern Jilin Province. Geotecton Metallog 40(5):1092–1106 **(in Chinese with English abstract)**

Wiedenbeck M, Hanchar JM, Peck WH, Sylvester P, Valley J, Whitehouse M, Kronz A, Morishita Y, Nasdala L, Fiebig J, Franchi I, Girard JP, Greenwood RC, Hinton R, Kita N, Mason PRD, Norman M, Ogasawara M, Piccoli PM, Rhede D, Satoh H, Schulz-Dobrick B, Skar O, Spicuzza MJ, Terada K, Tindle A, Togashi S, Vennemann T, Xie Q, Zheng YF (2004) Further characterization of the 91500 zircon crystal. Geostand Geoanal Res 28:9–39

Wu FY, Lin JQ, Wilde SA, Zhang XO, Yang JH (2005a) Nature and significance of the Early Cretaceous giant igneous event in Eastern China. Earth Planet Sci Lett 233:103–119

Wu FY, Yang JH, Liu XM (2005b) Geochronological framework of the Mesozoic granitic magmatism in the Liaodong Peninsula Northeast China. Geol J China Univ 11:305–317 **(in Chinese with English abstract)**

Wu FY, Walker RJ, Yang YH, Yuan HL, Yang JH (2006a) The chemical-temporal evolution of lithospheric mantle underlying the North China Craton. Geochim Cosmochim Acta 70:5013–5034

Wu FY, Yang YH, Xie LW, Yang JH, Xu P (2006b) Hf isotopic compositions of the standard zircons and baddeleyites used in U-Pb geochronology. Chem Geol 234:105–126

Wu FY, Xu YG, Gao S, Zheng JP (2008) Lithospheric thinning and destruction of the North China Craton. Acta Petrol Sinica 24:1145–1174 **(in Chinese with English abstract)**

Wu FY, Sun DY, Ge WC, Zhang YB, Grant ML, Wilde SA, Jahn BM (2011) Geochronology of the Phanerozoic granitoids in northeastern China. J Asian Earth Sci 41:1–30

Yang JH, Wu FY, Simon AW (2003) A review of the geodynamic setting of large-scale Late Mesozoic gold mineralization in the North China Craton: an association with lithospheric thinning. Ore Geol Rev 23:125–152

Yang JH, Wu FY, Shao JA, Simon AW, Xie LW, Liu XM (2006) Constrains on the timing of uplift of the Yanshan fold and thrust belt, North China. Earth Planet Sci Lett 246:336–352

Yuan HL, Gao S, Liu X, Liu XM, Li HM, Günther D, Wu FY (2004) Accurate U–Pb age and trace element determinations of zircon by laser ablation-inductively coupled plasma-mass spectrometry. Geostand Geoanal Res 28:353–370

Zhai MG, Zhu RX, Liu JM, Meng QR, Hou QL, Hu SB, Li Z, Zhang HF, Liu W (2003) The key period of Mesozoic tectonic regime transition in the eastern part of North China. Sci China (Ser D) 33:913–920 **(in Chinese)**

Zhang Q, Wang Y, Li CD, Wang YL, Jin WJ, Jia XQ (2006) Granite classification on the basis of Sr and Yb contents and its implications. Acta Petrol Sinica 22:2249–2269 **(in Chinese with English abstract)**

Zhang Q, Jin WJ, Li CD, Wang Y, Wang YL (2011) Granitic rocks and their formation depth in the crust. Geotecton Metallog 35:259–269 **(in Chinese with English abstract)**

Zheng JP, Griffin WL, O'Reilly SY, Yang JS, Li TF, Zhang M, Zhang RY, Liu JG (2006) Mineral chemistry of peridotites from Paleozoic, Mesozoic and Cenozoic lithosphere: constrains on mantle evolution beneath Eastern China. J Petrol 47:2233–2256

Zheng JP, Griffin WL, O'Reilly SY, Yu CM, Zhang HF, Pearson N, Zhang M (2007) Mechanism and timing of lithospheric modification and replacement beneath the eastern North China Craton: peridotitic xenoliths from the 100 Ma Fuxin basalts and a regional synthesis. Geochim Cosmochim Acta 71:5203–5225

Zhu G, Hu ZQ, Chen Y, Niu ML, Xie CL (2008) Evolution of early cretaceous extensional basins in the eastern North China craton and its implication for the craton destruction. Geol Bull China 27:1594–1604 **(in Chinese with English abstract)**